STScI | SPACE TELESCOPE SCIENCE INSTITUTE

WFC3 Instrument Science Report 2020-10

Updated WFC3/IR Photometric Calibration

V. Bajaj, A. Calamida, J. Mack

February 15, 2021

Abstract

We present the continued analysis of photometric measurements of the CALSPEC standard stars over the last 11 years in all of the 15 WFC3/IR filters. In general, the photometry (countrate) is consistent with the 2012 calibration to 1% or better. However, new models for the CALSPEC primary white dwarfs changed the HST photometric flux reference system, thus changing the inverse sensitivities and zeropoints. This change is less than 0.5% on average for the wide filters, but increases to just under 2% for the reddest medium and narrow filters. No discernible changes in sensitivity over time are detected in the measurements, but this is partially due to a lack of precision likely caused by persistence of previous observations, as well as other effects that are not currently well understood. The new zeropoint tables are presented here.

Introduction

The monitoring of the Wide Field Camera 3 Infrared (WFC3/IR) channel's photometric performance via the measurement of standard spectrophotometric stars has been continued since the launch of the instrument in 2009. The first 1.5 years of measurements were analyzed and presented in Kalirai et al. 2011. We present the continuation of that analysis for all relevant data taken up through August 2020. In particular, we analyze long-term changes to the sensitivity of the IR channel, as accurately quantifying the sensitivity of the instrument is crucial to the computation of the zeropoints. We also present some insights regarding the lower than expected precision of photometry with the IR channel. Furthermore, we discuss

the limitations to the photometric calibration due to the use of standard star images, and possible future studies that can be made to achieve increased precision. Lastly, we briefly discuss the impact of updated flatfield calibrations on the standard star images and the derived photometry.

Observations

Due to their highly stable nature, and well understood physics, the HST standard stars are observed by a large volume of both calibration and general observer proposals. We use all imaging data of these stars in this analysis, covering all 15 WFC3/IR filters, save for the cases in which the point spread function (PSF) falls off the boundary of the subarray of active pixels, or where the star is saturated. As some of the programs were not designed for photometric calibration purposes, the number of observations for each target, and filter is highly variable. The list of programs in which data were taken for each star is presented in Table 1.

Star	Proposal IDs
GD-153	11451, 11552, 11926, 12334, 12699, 12702, 13089, 13092, 13575, 13579, 13711, 14021, 14384, 14386, 14544, 14883, 14992, 14994, 15113, 15582, 16030
GD-71	11926, 11936, 12333, 12334, 12357, 12699, 12702, 13711, 14024, 14384, 14883, 14992, 15113, 15582, 16030
GRW+70 5824	11557, 12333, 12698, 13088, 13575, 15582, 16030
P330E	11451, 11926, 12334, 12699, 13089, 13573, 13575, 14021, 14328, 14384, 14883, 14992, 16030
G191B2B	11926, 12334, 13094, 13576, 13711, 15113

Table 1: Proposal IDs for observations used in these analyses. For more information, see the MAST archive.

The majority of the datasets used in this analysis were observed as part of photometric calibration programs, and typically feature large enough exposure times to exceed a signal-to-noise ratio (SNR) greater than 100. In more recent proposals (starting in 2017) the observations were designed with persistence mitigation techniques in mind. Specifically, frequent dithering to place the star on a recently unused portion of the detector was used to mitigate persistence. Reducing the effects of persistence is critical to achieving high precision photometry (Bajaj 2019).

Analysis

The data were downloaded from the MAST archive in August 2020 to ensure the most recent reference files were used. However, a new flatfield calibration was developed contemporaneously (Mack et. al, 2020, in prep) and the resultant new flat files were used in the calwf3

processing (see the "Effects of New Calibration" section). Images were then grouped by target and filter. Within those groups, images taken within the same visit were drizzled together, as images taken in the same visit typically have very precise relative astrometry. This served to reduce the number of discrepant artifacts in the images. Source finding was performed on these drizzled images using the python package photutils implementation of the DAOFIND algorithm (Stetson 1987). The DAOFIND full width at half max was set to the approximate width of the IR PSF of approximately 1.2 pixels. Though the FWHM varies slightly with filter pivot wavelength a parametrization with respect to wavelength was unnecessary for satisfactory results. Due to the highly undersampled nature of the IR PSF, many spurious sources would often be detected. In some cases, due to larger subarray usage and longer exposure times, other sources may also appear in the images, leading to extra detections.

To dispense of the superfluous detections, an initial pass of aperture photometry was performed on the images. The measured countrates were then compared to synthetic values computed by PySynphot, using empirical models of the standard stars and total system throughput curves. The object that reported the closest countrate to the synthetic countrate was used to record an approximate position of the standard star in each image. This proved to be the most successful out of many source detection methods that were implemented, as the synthetic flux values and photometric performance are consistent enough (within a few percent) to ensure an accurate selection.

The approximate positions from the drizzled images were then transformed back to the FLT image coordinate system via the `all_pix2world()` and `all_world2pix()` methods of the astropy WCS package (The Astropy Collaboration et al. 2018). The positions were then recentered in each image using 2D gaussian fitting to the central-most pixels of the PSF, ensuring that the small aperture used in the photometry is placed correctly. Typical aperture photometry is then performed on the pixel-area-map-corrected FLT images, using an aperture radius of 3 pixels (0.4") and a background annulus ranging from 15 to 30 pixels, using a sigma clipped median to calculate sky level. Unlike the analysis in Kalirai (2011), the pixel area map multiplication was necessary, as the placement of the stars on the images spanned much of the total detector area. Thus, the pixel area map was sliced to contain only the pixels used in each subarray image, and multiplied by the data array before photometry was performed. The aperture photometry was accomplished using photutils and the wfc3_photometry package (Bradley et al. 2017). Since the FLT images for the IR channel are already reduced to electrons per second, no further corrections were required. In Kalirai et al. 2011, the aperture radius of three pixels was used, but also was described as not being optimal for minimizing the dispersion of the measurements. However, in repeating this analysis with more data, we find that the three pixel aperture minimizes the standard deviation for the GD-153 (the most observed star of the set) flux measurements in both the F110W and F160W filters.

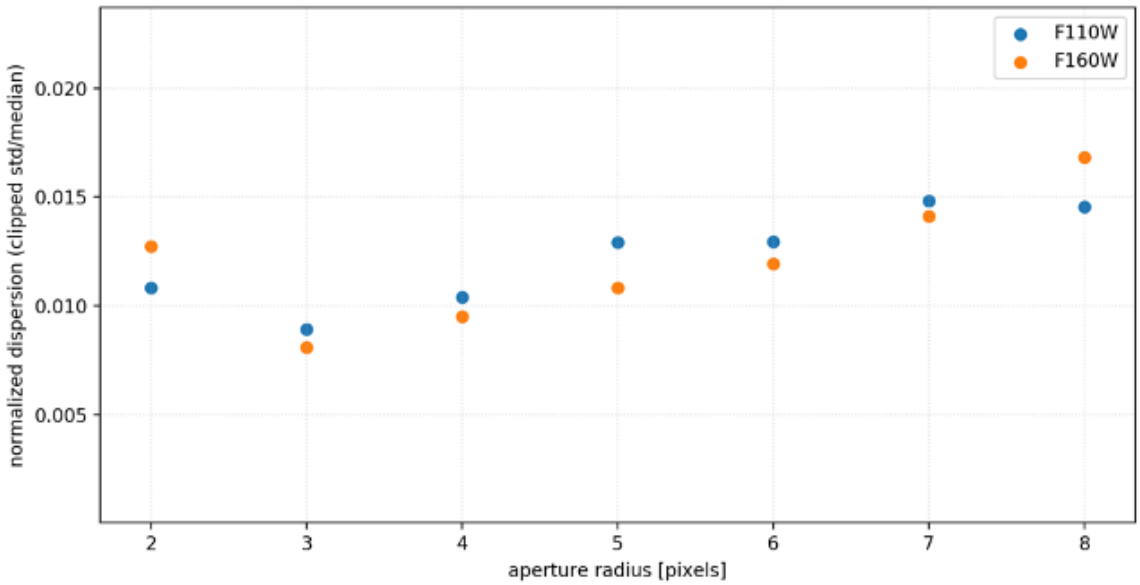

Figure 1: Comparison of the normalized standard deviation for F110W and F160W as a function of aperture radius. Since an aperture radius of three pixels minimized dispersion for both short and long wavelengths, this radius was used for all filters in the analysis

Photometry

In general, the photometry of the IR detector remains stable over time. The (three sigma) clipped standard deviation of the flux measurements of a given target/filter were normalized by the median flux measurement to compare the photometry across the various standards. This normalized standard deviation (in percent) is presented in Table 2. The updated zeropoints from these measurements are shown in appendix A, and lots showing photometry over time for all five standards in the 15 WFC3/IR filters are shown in appendix B.

Filter	GD-153	GD-71	P330E	GRW+70 5824	G191B2B
F098M	0.99	1.69	1.07	1.17	1.76
F105W	1.84	1.92	1.16	1.19	1.41
F110W	0.96	1.2	1.01	0.63	1.31
F125W	1.14	1.16	1.03	1.58	0.72
F126N	1.95	0.91	1.05	0.65	0.22*
F127M	1.19	1.03	0.98	0.83	1.36
F128N	1.77	0.94	1.26	0.59	0.1*
F130N	2.3	0.84	1.16	0.39	0.13
F132N	2.49	0.96	1.19	0.29	0.01*
F139M	1.69	0.93	1.0	0.99	0.99
F140W	0.94	1.22	0.88	0.72	0.89
F153M	1.59	0.75	0.71	0.6	0.72
F160W	0.85	0.96	0.92	0.72	0.71
F164N	2.13	1.13	1.14	0.47	0.18*
F167N	2.04	1.04	1.07	0.63	0.05*

Table 2: The normalized standard deviation of the photometric measurements of the standard stars, in percent. The entries labeled with "*" have less than 3 data points, and should not be considered as meaningful.

The Search for Systematics

While the dispersion for many of the filters is fairly small (less than 1%), the signal-to-noise ratio of many of the observations is often substantially larger than 100, even including noise imparted from calibration (as reported in the error array of the FLT images). Figure 2 shows the how the dispersion of photometry evolves with signal to noise ratio (flux divided by photometric error) of the exposures. Notably, the actual standard deviations are consistently higher than predicted for all SNR levels.

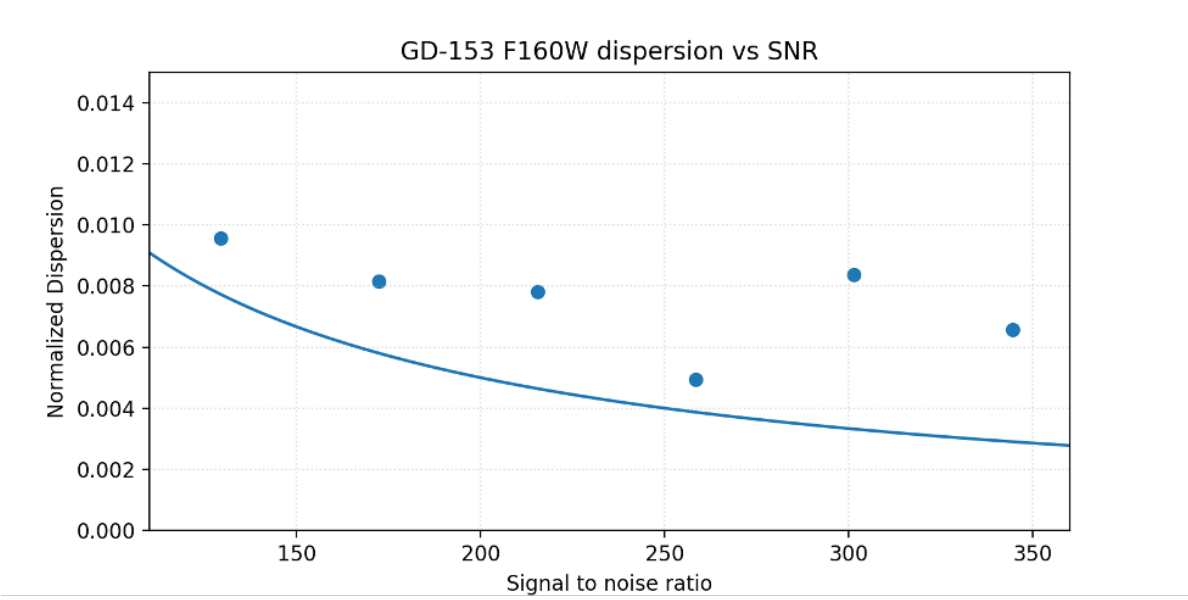

Figure 2: The normalized standard deviation (in percent) of photometric measurements of GD-153 vs signal-to-noise ratio. The blue line represents the expected normalized standard deviation (1/SNR).

In some cases, inclusion of images taken with different observation strategies imparts a higher dispersion onto the photometry. Some of the observations of GD-153 F105W, for example, were used in the WFC3/IR grism calibration and only include a small number of reads per exposure, resulting in much more noisy data, due to the poorly understood behavior of the first read of WFC3/IR integrations (see Figure 3). Removing these low sample exposures from the analysis increases precision for a small subset of the filters, though not to the level predicted by the SNR. In the example of the GD-153/F105W images with less than 6 reads have a clipped standard deviation of 2%, while those with more reads have a much smaller dispersion of 0.7%. In addition, the difference between the means of the two populations differ by approximately 1.3%. However, this does not always yield a more precise result, and actually increases the dispersion for some other target/filter combinations.

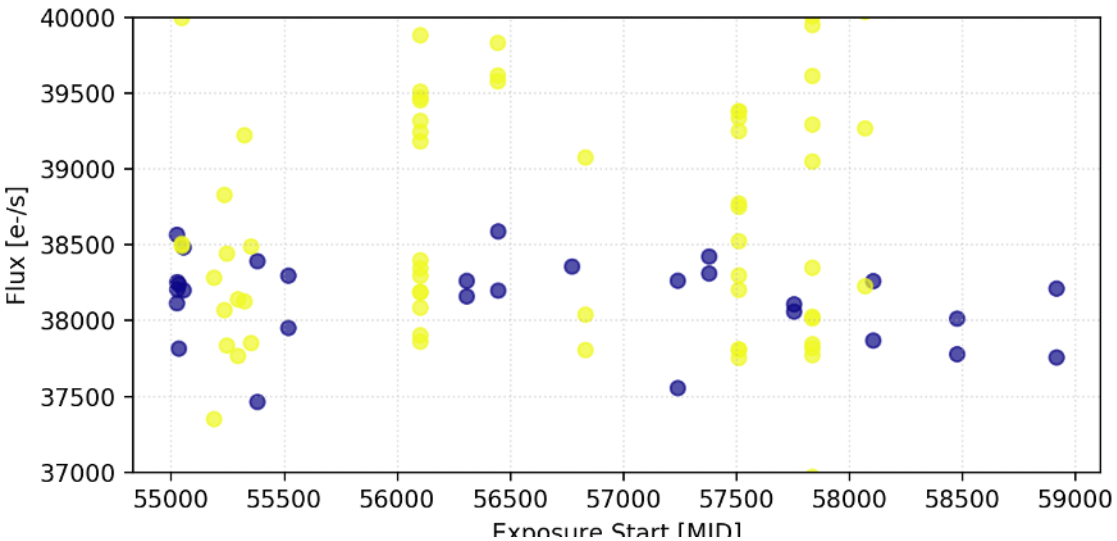

Figure 3: : Flux of GD-153 taken in F105W. Points are color coded by number of samples (nsamp). The yellow points are NSAMP <6, while purple are NSAMP $\geq$ 6.

As noted in Bajaj (2019), the effects of persistence (afterglows of bright sources observed in preceding images) significantly lower the precision for WFC3 IR observations. This is likely due to the dependence of persistence signals on time from the stimulus (the exposures that caused the persistence), and fluence of the previous exposures causing the persistence (Long, Baggett, and Mackenty 2013). Additionally, longer term persistence (from observations up to days before) can sometimes still affect the standard star observations (Ryan and Baggett 2015), though this effect is generally smaller than the "self persistence" (persistence from observations in the same visit). The excess flux from persistence is thus not well constrained, and is virtually indistinguishable from real flux. The variability of persistence is one of the causes of the lower than expected precision. Because the effects of persistence on precision photometry were not initially well understood, many of the earlier observations of the standard stars dither infrequently, and sometimes only by a few pixels. While this may maximize observational efficiency, it incurs a loss of precision. Frequent, large dithers can mitigate much of the effect of the persistence and lead to substantially better precision,

and are therefore used in photometric calibration programs since 2017. .

However, the WFC3/IR detector also exhibits longer term behavior, where even the first observations in a visit (which should be unaffected by persistence) show photometric offsets compared to previous visits (Bajaj 2019). In some cases, these offsets are present across a visit. The visit-to-visit variation is distinct from the Poisson error, as Poisson errors manifest randomly. This effect is also detected in spatial scan data, where Poisson noise terms are effectively 0 (Som 2020, in prep). This instability between visits is not currently well understood.

Effects of New Calibration

An additional factor that differentiates this analysis and the resulting zeropoints from those of Kalirai et al. 2011 is the new calibration. The updated flat fields described in Mack et. al (2020, in prep.), while incorporating more data, do not substantially reduce the scatter of the measurements. This is partially due to the clustering of observations of the standard stars near the center of the detector (as WFC3/IR subarrays are centered on the array). The error in the flatfield in the center of the detector was already below the half percent level (Dahlen 2013), and thus the change in the new flats pixel to pixel variation is minimal. However, a change to the normalization of the flats causes a 0.1% drop in calibrated count rates, which is compensated for via a corresponding change in the zeropoint. Thus, when the zeropoint is applied, the measured flux is the same between calibration versions.

Though the photometry is consistent with the results of Kalirai et al. 2011, the zeropoints for WFC3/IR change by a small amount due to recomputation of the synthetic models of the standard white dwarf stars. A small, wavelength-dependent update to the CALSPEC models yields a slightly different zeropoint, as it represents a change of the physical flux incident on the detector (Bohlin, Hubeny, and Rauch 2020). Though the change in the zeropoints would appear to show a loss of sensitivity (a brighter magnitude), it should be interpreted as a more accurate, higher physical flux estimate of the sources measured, and not a sensitivity loss. The total change of the zeropoints is presented in Figure 4.

Discussion and Supplemental Studies

The overall stability of the detector appears to remain similar to the results found in Kalirai et al. 2011, with a typical dispersion of $\sigma \approx 1\%$ and no significant trends consistent across targets or fiilters. However, lack of precision and nonrepeatability of the photometric measurements ultimately limit the ability to detect the small sensitivity losses on the order of those seen in other HST instruments. Specifically, the visit-to-visit variation of the photometry substantially reduces the precision of any time dependent measurement of the sensitivity. Thus, the measurements taken in the WFC3/IR sensitivity monitoring programs are unable to support the findings seen in other studies such as Kozhurina-Platais and Baggett 2020, which seem to detect sensitivity losses on the order of 1-3% over 10 years using observations of the core of Omega Centauri.

A portion of the nonrepeatability may be attributed to varying observation configurations (e.g. different sample sequences, number of samples, and exposure time). A substantial

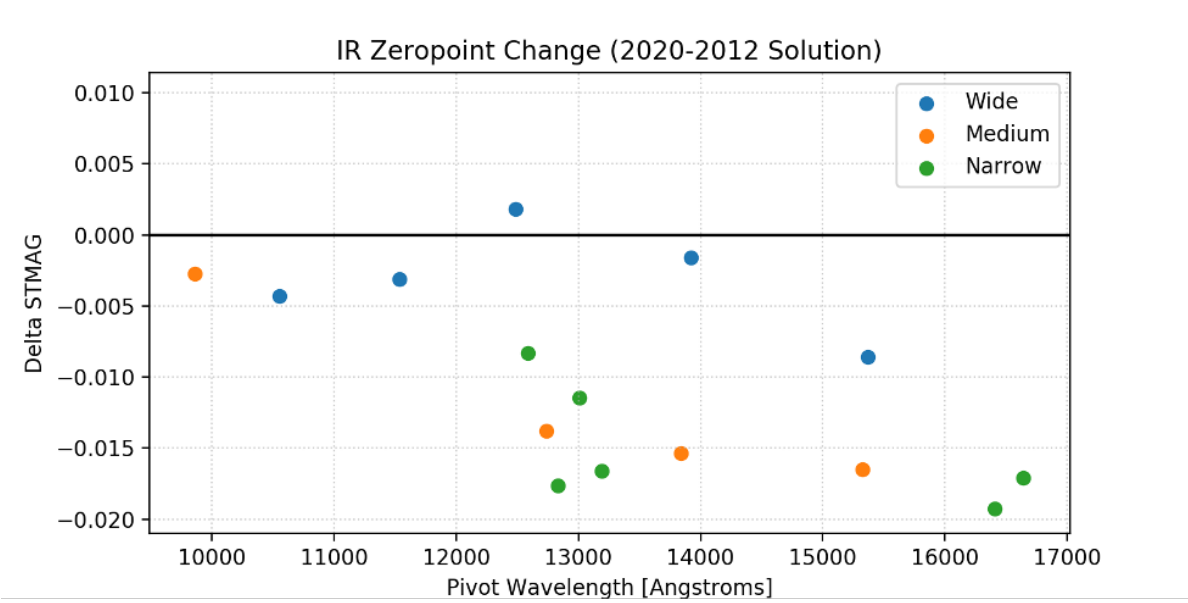

Figure 4: : Change in the STMAG zeropoints for WFC3/IR. The systematically larger change in the redder wavelengths is primarily due to the new synthetic models.

detection or correction of systematic behavior as a function of these observation characteristics would likely require additional, extensive processing in the calibration pipelines. The dependence of the photometry on these characteristics is currently being investigated.

Current calibration programs seek to measure sensitivity losses via spatial scanning, as this observation strategy allows for extremely small Poisson noise terms. However, preliminary analysis shows uncertainties much larger than the Poisson noise would predict within a visit, and from visit to visit (Som, 2020 in prep). This effect is not persistence related also not currently well understood, but appears consistent with the visit to visit variability of the standard star measurements. However, these observations were designed to limit persistence effects, and have a much more unified observation strategy (compared to the standard star observations), reducing parameter space in the analysis of systematics.

Observations of other, less crowded stellar clusters with well designed, consistent strategies between epochs may yield more precise measurements of sensitivity losses, and are being considered for future calibration cycles. We also seek to support measurements of the time-dependent sensitivity via analyses of archival data, though heterogeneity in observation targets and strategies may limit the efficacy of those studies.

Updated Calibration Reference Files

The changes to the calibration of WFC3/IR data are encapsulated in subset of the reference files available in the Calibration Reference Data System (CRDS). The new flatfield calibrations are stored in new `PFLTFILE` (pixel-to-pixel flat file) and `DFLTFILE` (delta flat file, storing information for the time dependent IR blobs) files. More information about these files is available in Mack et. al (2020, in prep). The new zeropoints are stored in

a new Image Photometry Table (`IMPHTTAB`) as inverse sensitivities (PHOTFLAM). Note that these zeropoints are computed for a photometric aperture of infinite radius. These files are necessary for data recalibration consistent with the new zeropoints. The new reference file, `4af1533ai_imp.fits`, is now available on the HST CRDS website. To maintain consistency with the `IMPHTTAB`, the filter curves used in the construction of bandpasses for synthetic photometry (PySynphot/STSynphot) were updated to reflect the new sensitivity. More information regarding the download of these files is available here. The models of the standard stars used (Bohlin, Hubeny, and Rauch 2020) in this analysis were also updated and placed in the CALSPEC data repository, and are available here. Note that these files are not necessary for the recalibration of images, and are solely for synthetic photometry.

Acknowledgements

We thank A. Calamida, H. Khandrika, J. Mack, J. Medina, and D. Som of the WFC3 Photometry Calibration group for their suggestions regarding analysis contained in and clarity of this report. We also thank J. Green for his review of this document.

References

Bajaj, V.. (June 2019). *WFC3/IR Photometric Repeatability*. WFC3 ISR 2019-07.

Bohlin, Ralph C., Ivan Hubeny, and Thomas Rauch (July 2020). "New Grids of Pure-hydrogen White Dwarf NLTE Model Atmospheres and the HST/STIS Flux Calibration". In: 160.1, 21, p. 21. DOI: 10.3847/1538-3881/ab94b4. arXiv: 2005.10945 [astro-ph.SR].

Bradley, Larry et al. (Oct. 2017). *astropy/photutils: v0.4*. DOI: 10.5281/zenodo.1039309. URL: https://doi.org/10.5281/zenodo.1039309.

Dahlen, T. (Jan. 2013). *WFC3/IR Spatial Sensitivity Test*. WFC3 ISR 2013-01.

Kalirai, J. et al. (Feb. 2011). *The Photometric Performance of WFC3/IR: Temporal Stability Through Year 1*. WFC3 ISR 2011-08.

Kozhurina-Platais, V. and S. Baggett (Apr. 2020). *WFC3 IR sensitivity over time*. WFC3 ISR 2020-05.

Long, K., S. Baggett, and J. Mackenty (July 2013). *Characterizing Persistence in the WFC3 IR Channel: Finite Trapping Times*. WFC3 ISR 2013-06.

Ryan, R. and S. Baggett (July 2015). *The Internal Flat Fields for WFC3/IR*. WFC3 ISR 2015-11.

Stetson, Peter B. (Mar. 1987). "DAOPHOT: A Computer Program for Crowded-Field Stellar Photometry". In: 99, p. 191. DOI: 10.1086/131977.

The Astropy Collaboration et al. (Jan. 2018). "The Astropy Project: Building an inclusive, open-science project and status of the v2.0 core package". In: *ArXiv e-prints*. arXiv: 1801.02634 [astro-ph.IM].

Appendices

A Zeropoints

Filter	Pivot	PhotBW	ABMag	Vegamag	STmag	mag error	PHOTFLAM
F098M	9864.72	500.85	25.6661	25.0984	26.9445	0.008	6.0653e-20
F105W	10551.05	845.62	26.2637	25.6122	27.6882	0.0047	3.0507e-20
F110W	11534.46	1428.48	26.8185	26.0528	28.4364	0.0046	1.5318e-20
F125W	12486.06	866.28	26.2321	25.3248	28.0221	0.0078	2.2446e-20
F126N	12584.89	339.31	22.8491	21.9218	24.6563	0.0079	4.9671e-19
F127M	12740.29	249.56	24.6246	23.6572	26.4584	0.0122	9.4524e-20
F128N	12831.84	357.44	22.9561	21.9129	24.8055	0.0078	4.348e-19
F130N	13005.68	274.24	22.9813	21.999	24.8599	0.0081	4.1416e-19
F132N	13187.71	319.08	22.9325	21.9289	24.8413	0.0071	4.2096e-19
F139M	13837.62	278.02	24.4663	23.3815	26.4796	0.0043	9.3134e-20
F140W	13922.91	1132.38	26.4502	25.3676	28.4768	0.0068	1.4759e-20
F153M	15322.05	378.95	24.4469	23.187	26.6815	0.006	7.7161e-20
F160W	15369.18	826.25	25.9362	24.6785	28.1774	0.0086	1.9429e-20
F164N	16403.51	700.06	22.8921	21.5013	25.2748	0.0121	2.8257e-19
F167N	16641.6	645.24	22.9366	21.5686	25.3505	0.0095	2.6215e-19

Table 3: The updated WFC3/IR zeropoints. The pivot and PhotBW columns are in Angstroms, while the PHOTFLAM column is in ergs/(cm^2*Angstrom*s*e^-)

B Photometry plots

In the following plots, five panels represent flux measurements for G191B2B, GD-153, GD-71, GRW+70 5824, and P330E, respectively. The measurements have been normalized by dividing the flux measurements by the median for that star/filter.

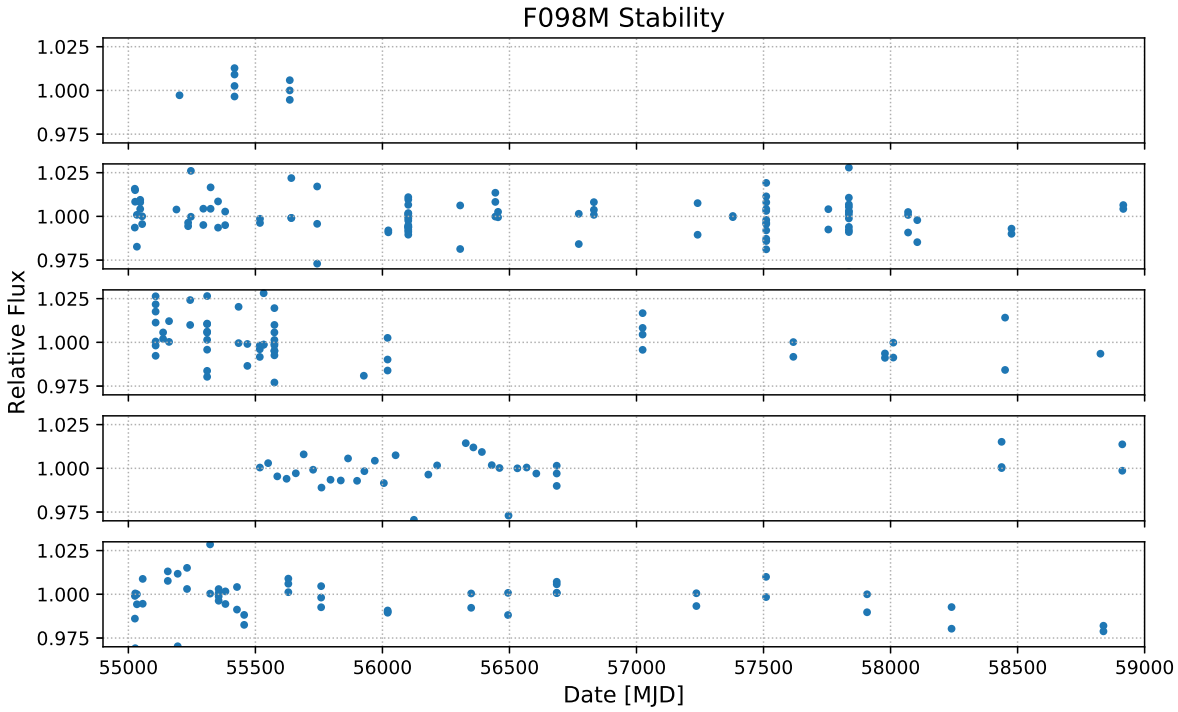

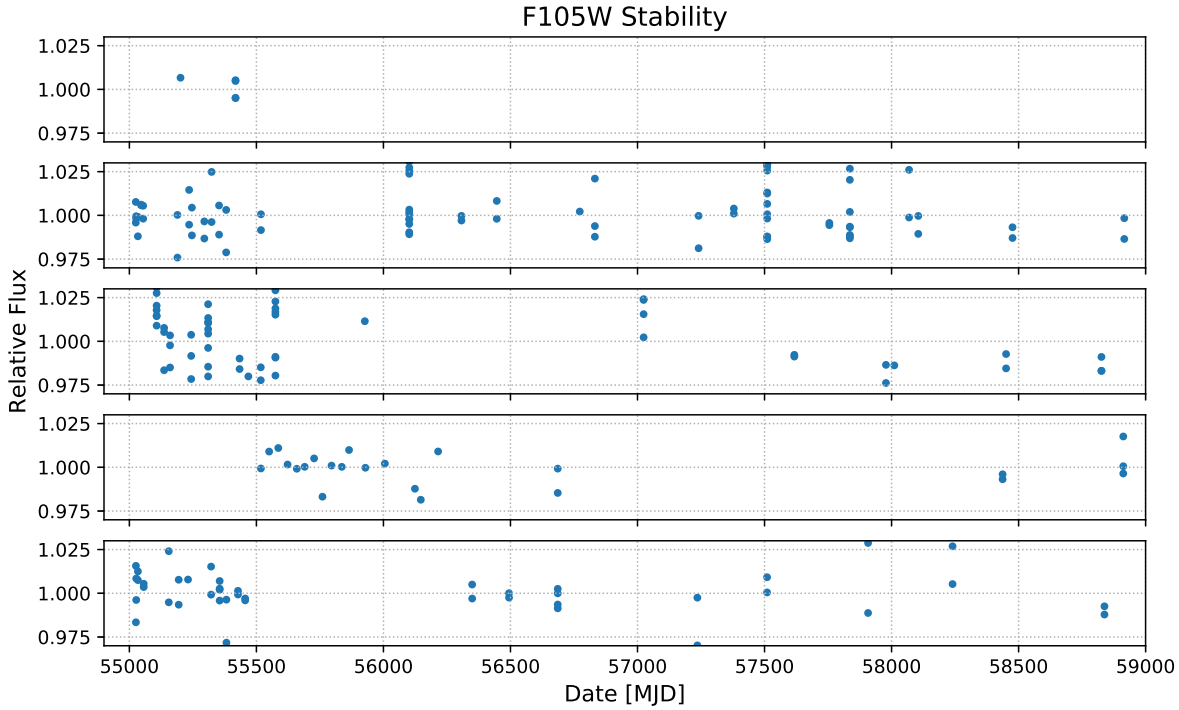
F105W Stability
Relative Flux
1.025
1.000
0.975
55000
55500
56000
56500
57000
57500
58000
58500
59000
Date [MJD]

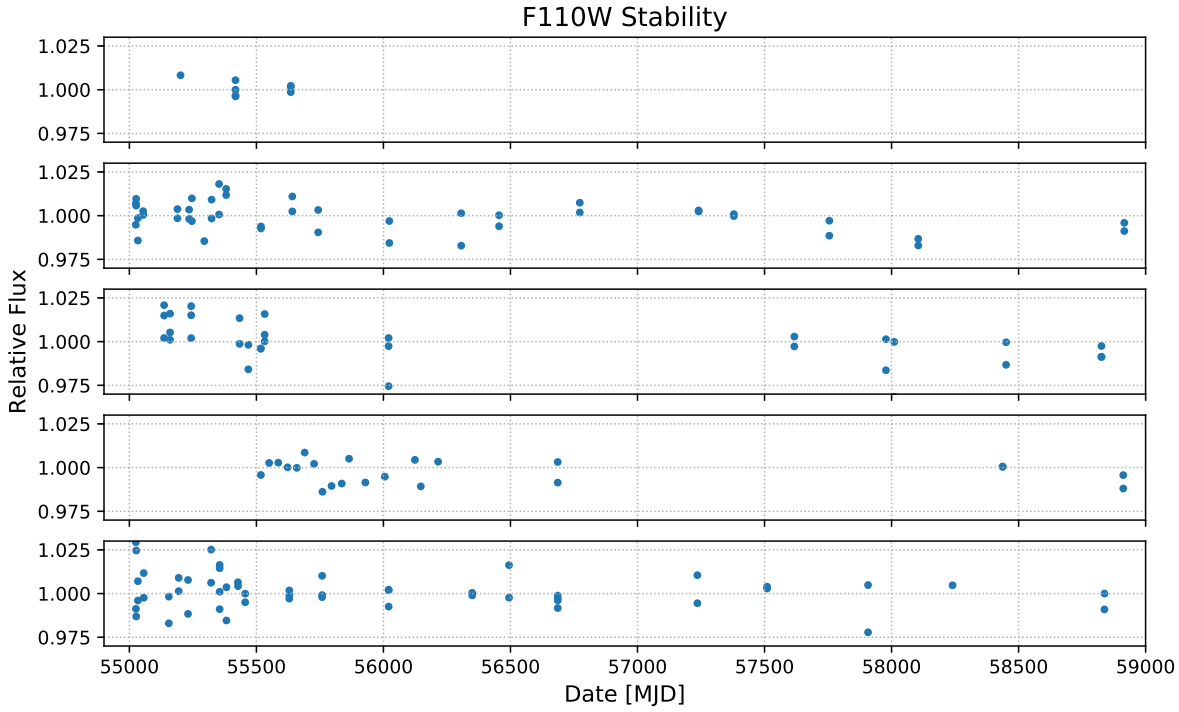
F110W Stability
Relative Flux
1.025
1.000
0.975
55000
55500
56000
56500
57000
57500
58000
58500
59000
Date [MJD]

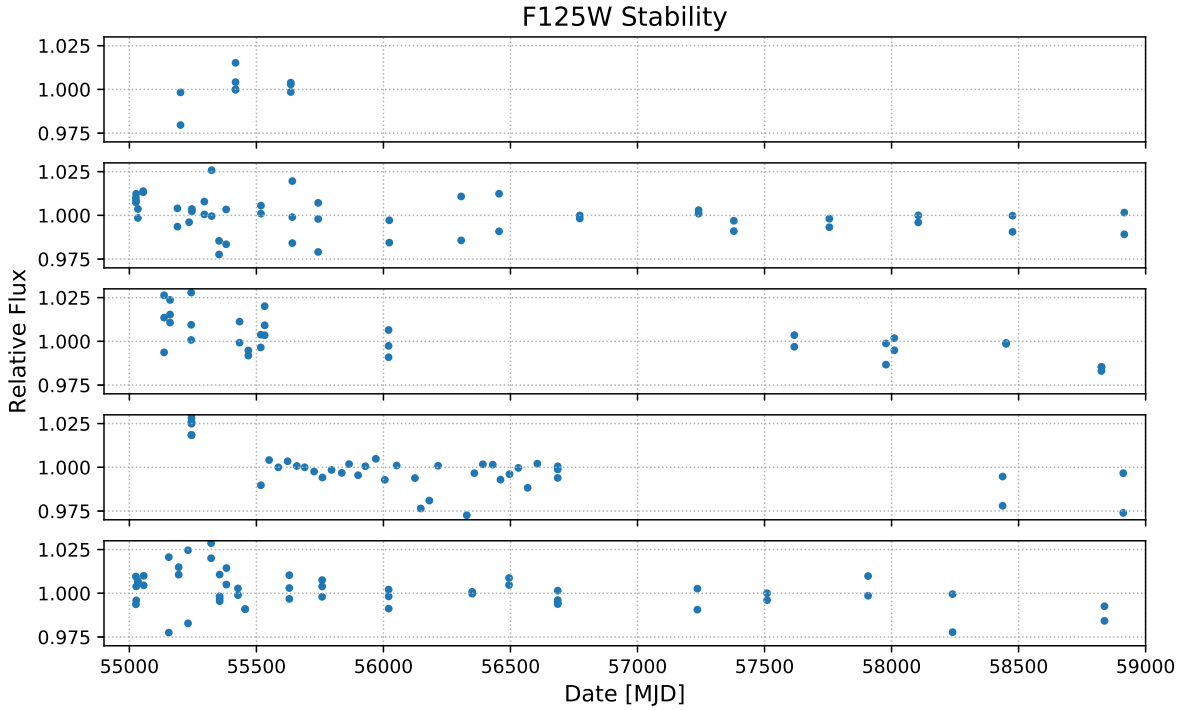
F125W Stability
Relative Flux
1.025
1.000
0.975
55000
55500
56000
56500
57000
57500
58000
58500
59000
Date [MJD]

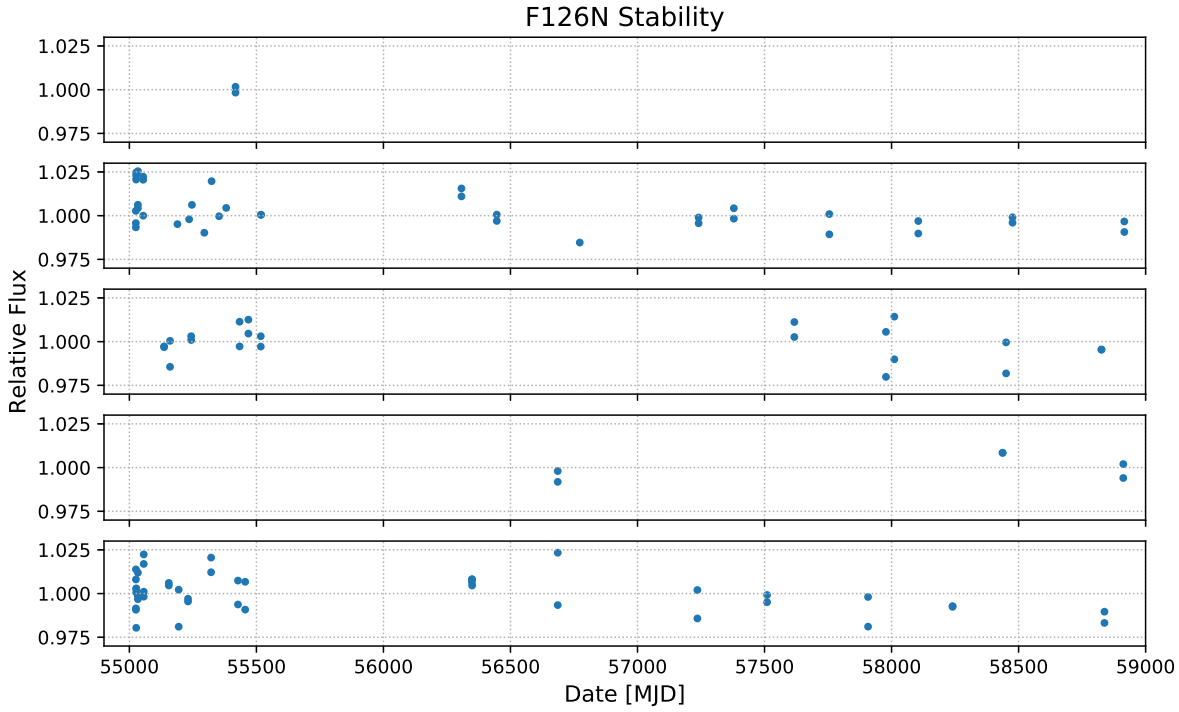
F126N Stability
Relative Flux
1.025
1.000
0.975
55000
55500
56000
56500
57000
57500
58000
58500
59000
Date [MJD]

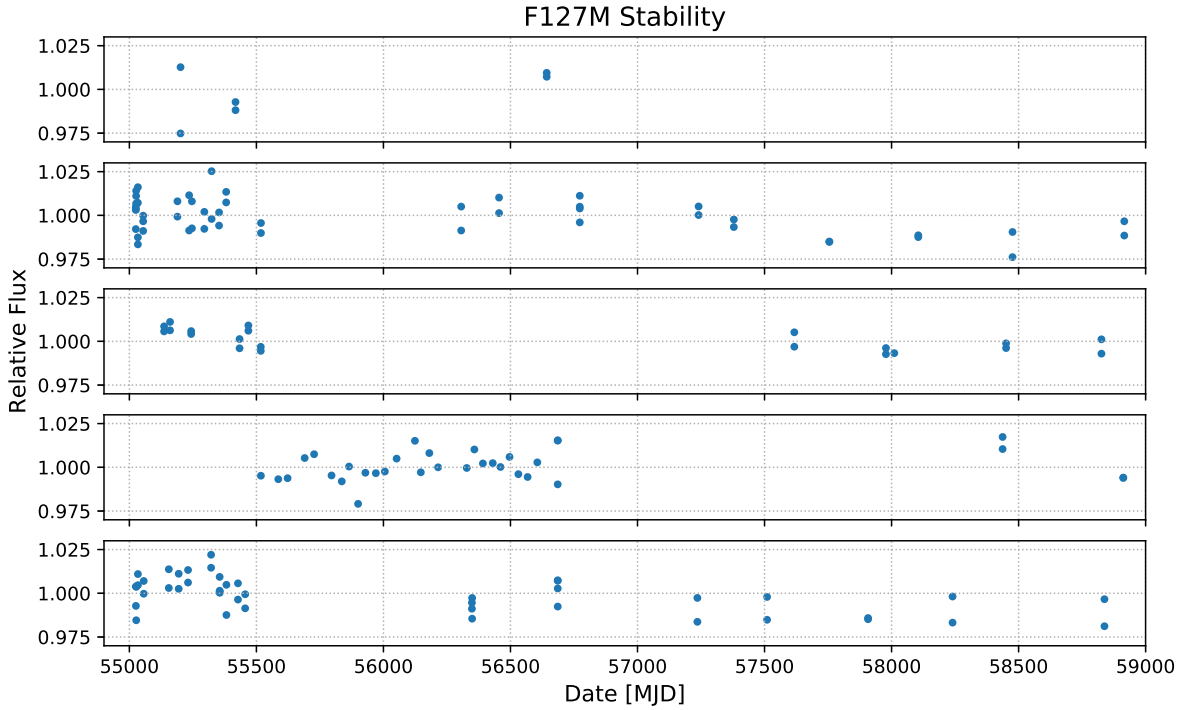
F127M Stability
Relative Flux
1.025
1.000
0.975
55000
55500
56000
56500
57000
57500
58000
58500
59000
Date [MJD]

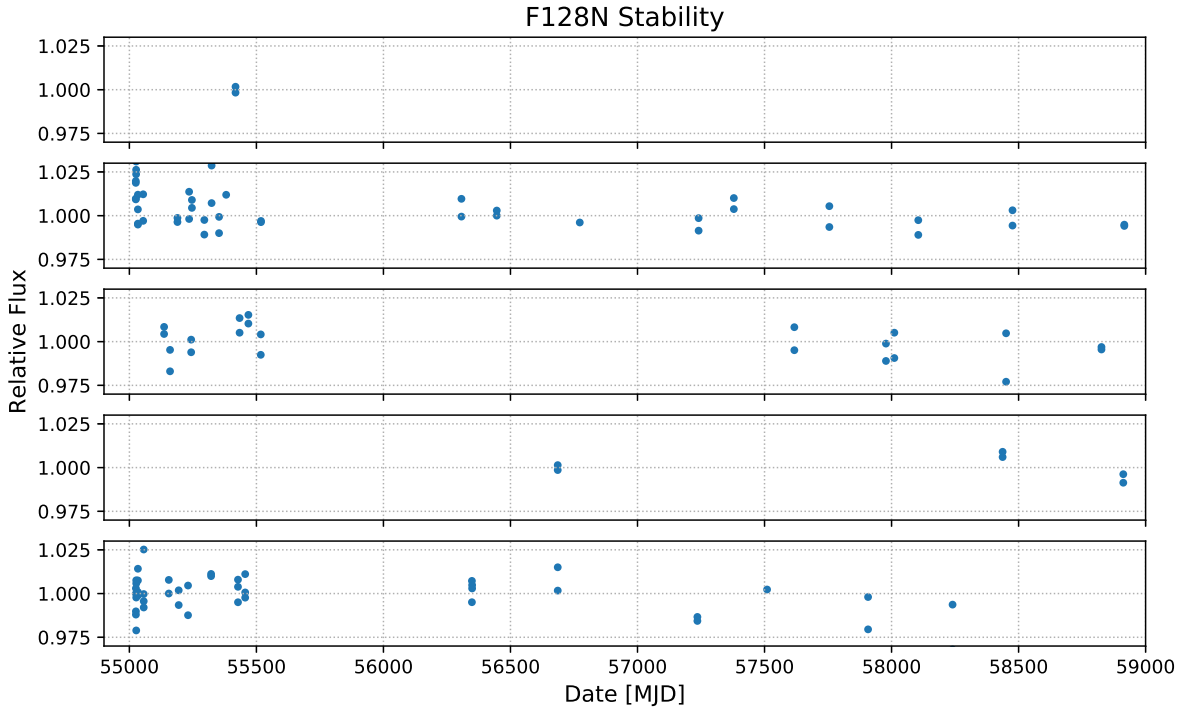
F128N Stability
Relative Flux
1.025
1.000
0.975
55000
55500
56000
56500
57000
57500
58000
58500
59000
Date [MJD]

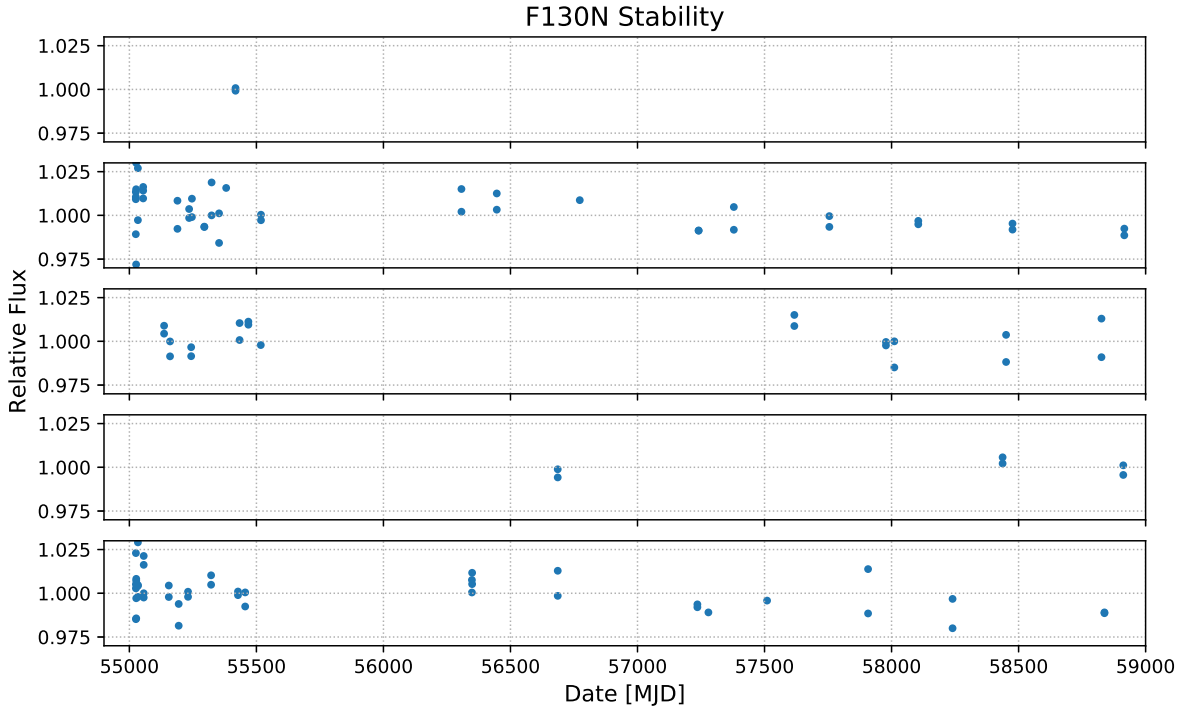
F130N Stability
Relative Flux
1.025
1.000
0.975
55000
55500
56000
56500
57000
57500
58000
58500
59000
Date [MJD]

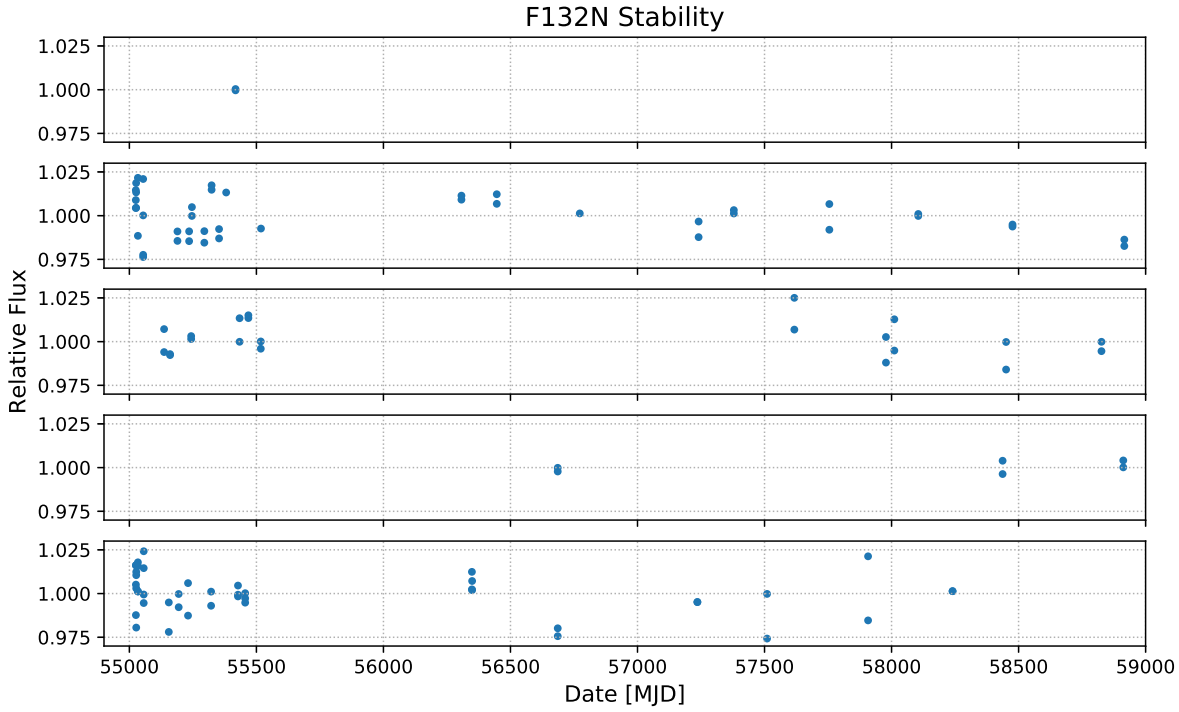
F132N Stability
Relative Flux
1.025
1.000
0.975
55000
55500
56000
56500
57000
57500
58000
58500
59000
Date [MJD]

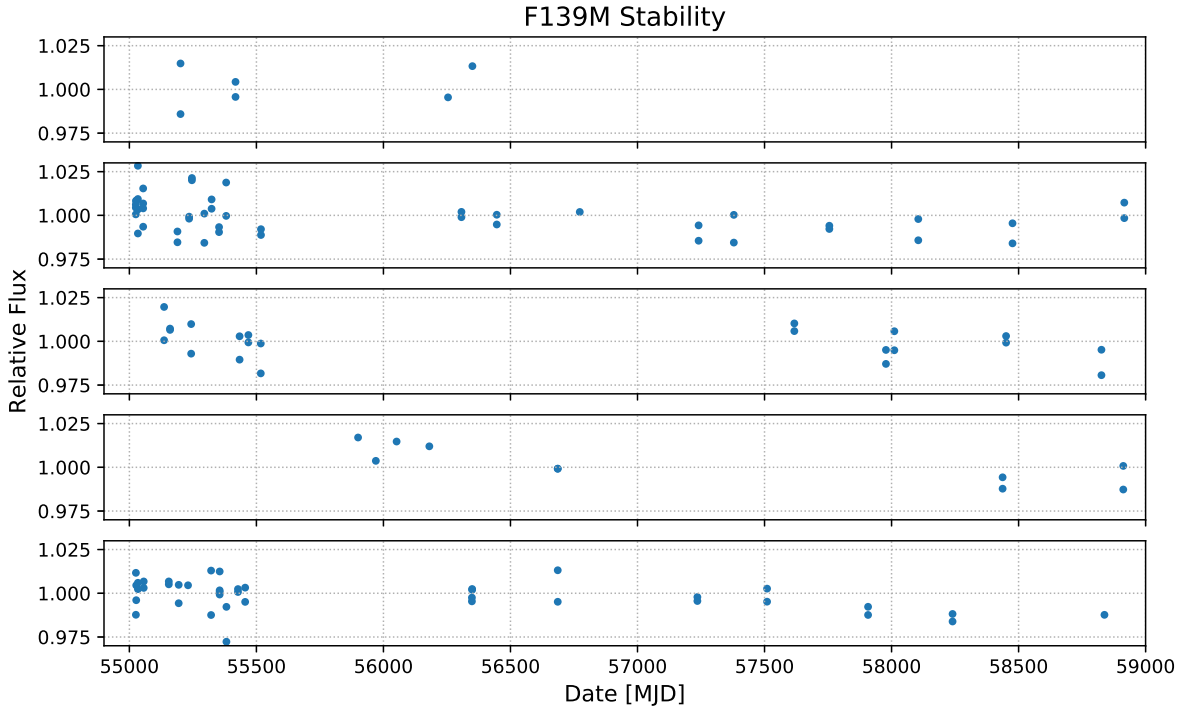
F139M Stability
Relative Flux
1.025
1.000
0.975
55000
55500
56000
56500
57000
57500
58000
58500
59000
Date [MJD]

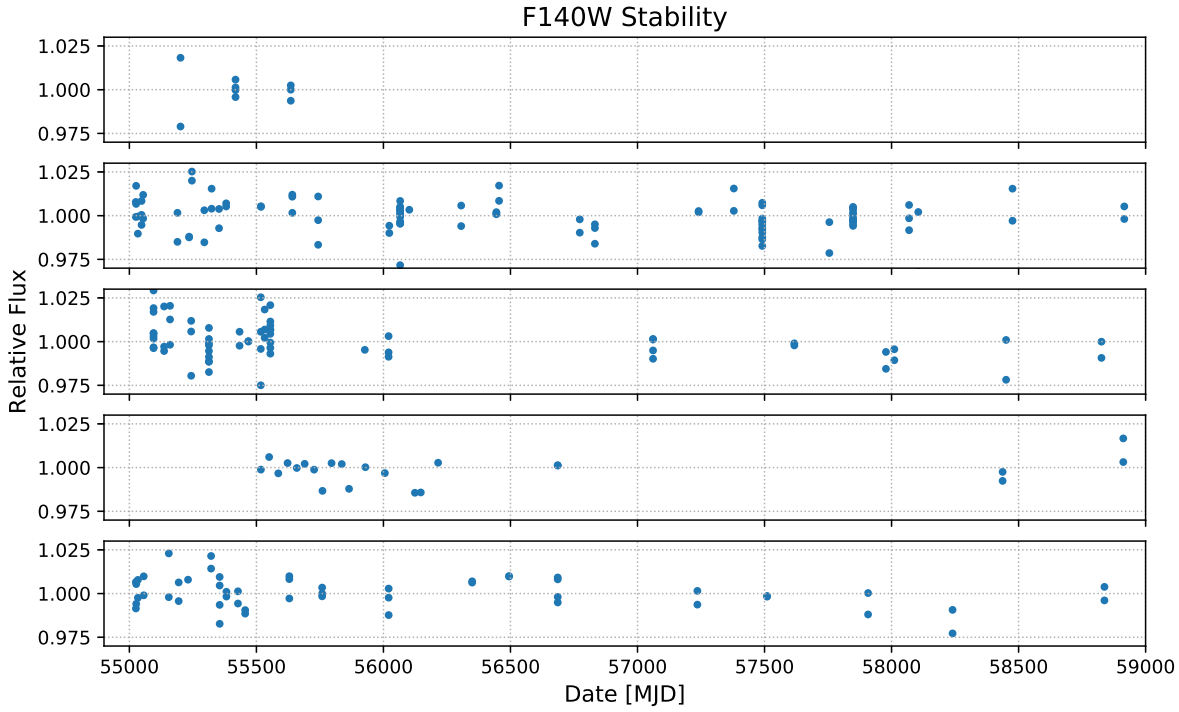
F140W Stability
Relative Flux
1.025
1.000
0.975
55000
55500
56000
56500
57000
57500
58000
58500
59000
Date [MJD]

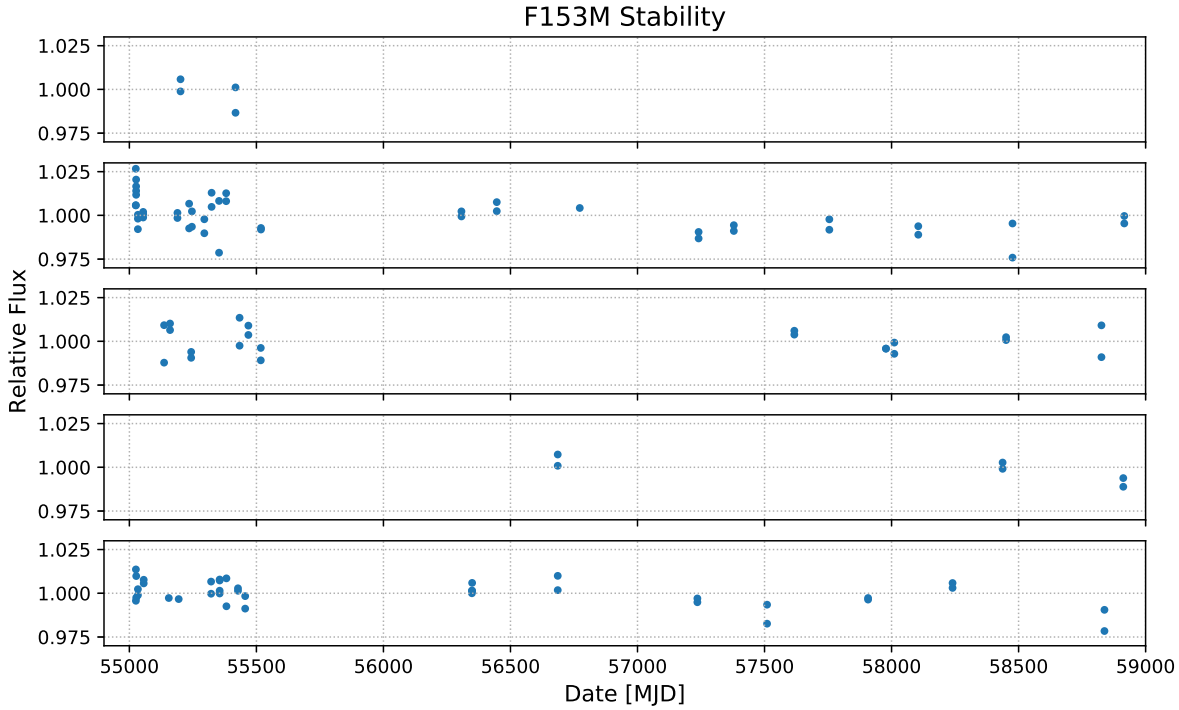
F153M Stability
Relative Flux
1.025
1.000
0.975
55000
55500
56000
56500
57000
57500
58000
58500
59000
Date [MJD]

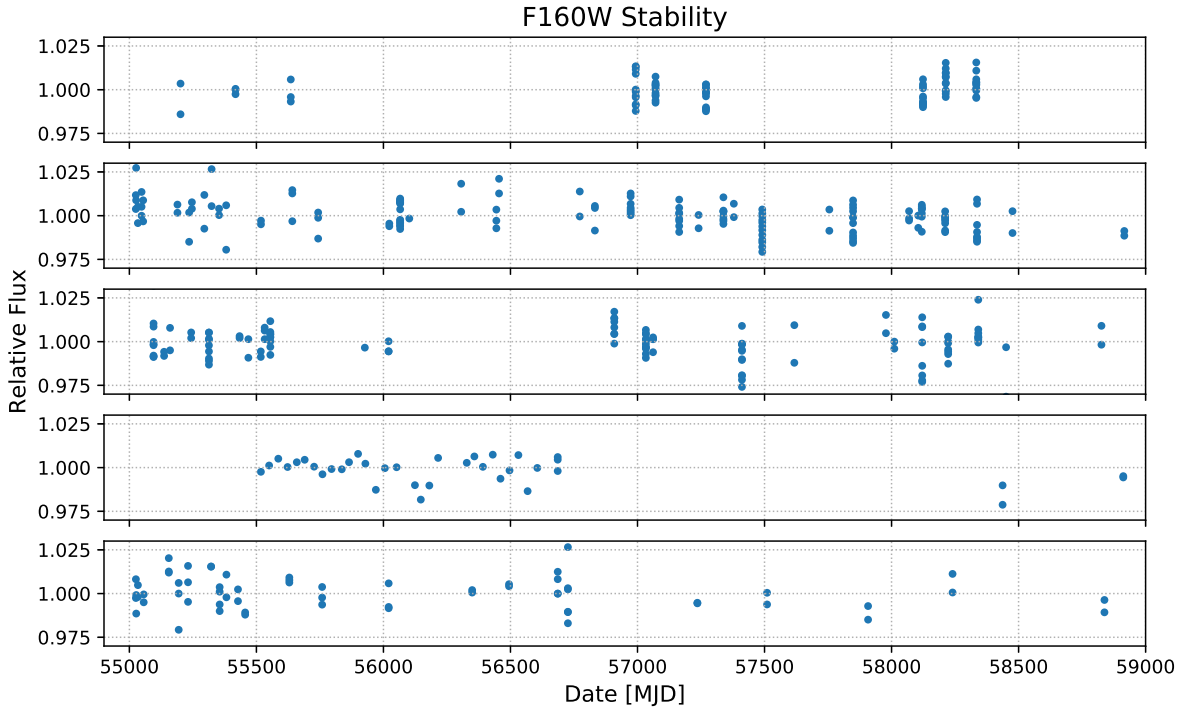
F160W Stability
Relative Flux
1.025
1.000
0.975
55000
55500
56000
56500
57000
57500
58000
58500
59000
Date [MJD]

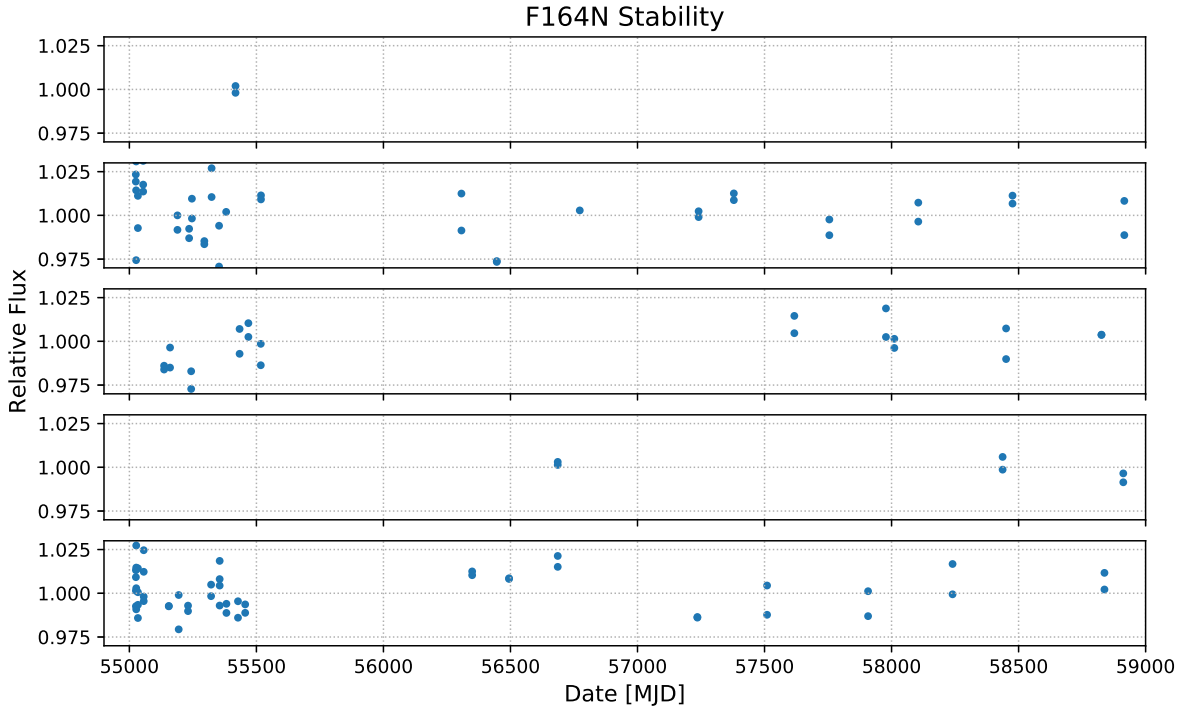
F164N Stability
Relative Flux
1.025
1.000
0.975
55000
55500
56000
56500
57000
57500
58000
58500
59000
Date [MJD]

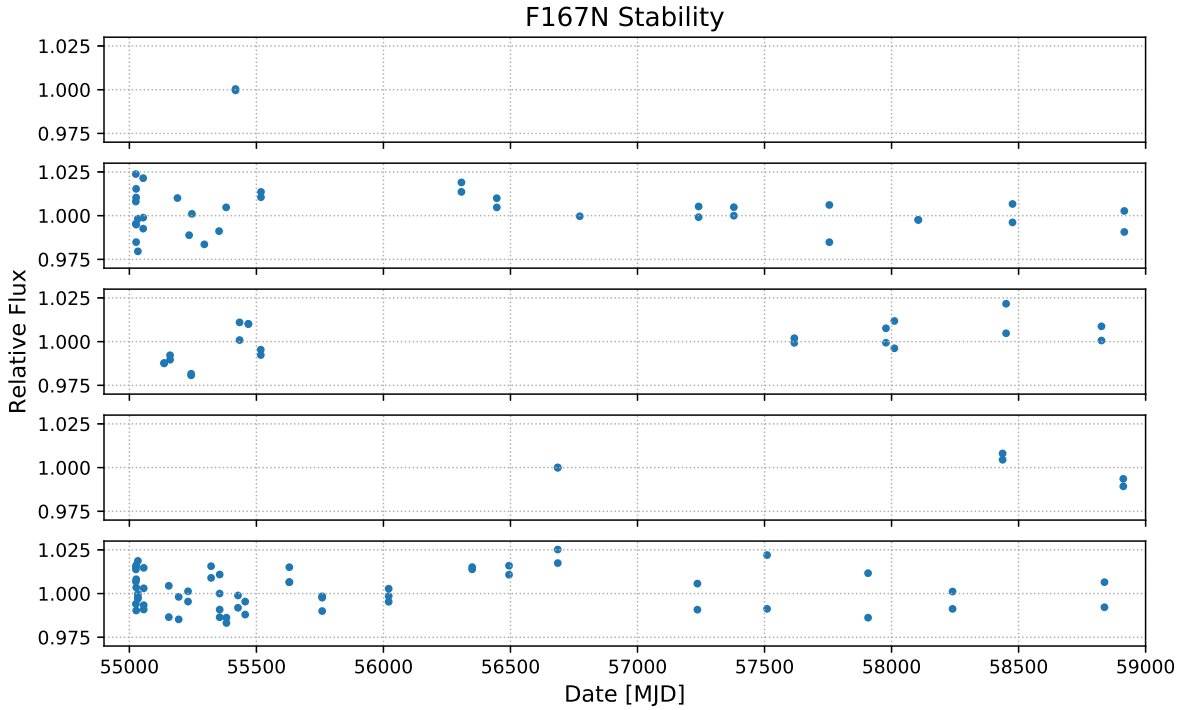
F167N Stability
Relative Flux
1.025
1.000
0.975
55000
55500
56000
56500
57000
57500
58000
58500
59000
Date [MJD]